ABCD-Based Melanoma Detection in Non-dermoscopic RGB Imaging

Maria Oniga(✉), Paul Florin Rus, and Alina Elena Sultana

National University of Science and Technology POLITEHNICA Bucharest, Bucharest 060042, Romania
{maria.oniga,alina_elena.sultana}@upb.ro, paul_florin.rus@stud.acs.upb.ro

Abstract. Melanoma is a highly aggressive skin cancer whose prognosis strongly depends on early detection. The ABCD rule of dermatology provides a clinically interpretable framework for lesion assessment based on asymmetry, border irregularity, color variation, and diameter. However, most existing computational implementations rely on dermoscopic images acquired under controlled conditions, limiting their applicability in real-world settings.

In this work, we propose a computational framework for the extraction of ABCD features from non-dermoscopic images captured using a standard RGB camera at a fixed distance. The proposed method includes an illumination correction pipeline, localization of the lesion, and mask creation. In addition, the study includes a color model derived from dermoscopic images based on color quantization and hybrid color classification, which adapts to the used dataset. The asymmetry and border irregularity scores were computed using geometric descriptors, while the diameter was determined as a feature and converted into mm.

The four features obtained were further used to create an adapted Total Dermoscopic Score (TDS), which classifies the skin lesions as benign, dysplastic, or malignant. The proposed approach was evaluated on a proprietary dataset of 146 images obtained using a standard camera. The overall accuracy obtained was 70.55%, which demonstrates that the ABCD rule can be adapted to standard RGB imaging, providing a low-cost alternative for melanocytic lesions in non-dermoscopic conditions.

1 Introduction

Melanoma is an aggressive form of skin cancer that arises from abnormal proliferating pigment-producing cells named melanocytes. [11]. Currently, this skin disease is a public health concern, whose incidence and mortality are increasing at an alarming rate [10]. According to the World Health Organization, in 2022, melanoma was diagnosed in 331,722 new cases and was responsible for 58,667 deaths globally, with a 2025 projection of 1,092,818 new cases in 2025 [4]. Thus, early detection is essential to reduce mortality rates.

Melanocytic lesions are diagnosed through dermoscopy, an examination using adequate illumination and magnification [14]. This technique is an essential tool

© The Author(s), under exclusive license to Springer Nature Switzerland AG 2027
O. Gervasi et al. (Eds.): ICCSA 2026, LNCS 16769, pp. 53–70, 2027.
https://doi.org/10.1007/978-3-032-30494-0_4

for lesion differentiation, which enhances the visualization of superficial and subsurface structures and improves diagnostic accuracy. Dermoscopes use polarized light to reduce reflection and enhance contrast, facilitating the visualization of diagnostically relevant features [5].

From a clinical perspective, melanoma is a pigmented lesion that is characterized by changes in size, shape, and color. These features are determined by the ABCDE criteria (Asymmetry, Border irregularity, Color variation, Diameter, and Dermoscopic features and Evolution), which guide the initial lesion assessment [3]; however, histopathological examination remains the preferred method to determine the final diagnosis [14].

The four criteria from the ABCD rule are used to determine the Total Dermoscopic Score (TDS), which provides a standardized pipeline for classifying skin lesions as benign, suspicious, or malignant. Thus, it is employed frequently in computer-aided diagnosis systems, where it enables quantitative analysis of specific features and improves diagnostic accuracy [2].

Recent studies on automated melanoma detection can be broadly categorized based on the type of imaging modality used and the level of interpretability of the extracted features.

Several studies rely on dermoscopic images, where controlled acquisition conditions and magnification facilitate the extraction of clinically meaningful structures. In this setting, several classical image-processing approaches quantify the ABCD rule. Study [16] computes asymmetry via vertical/horizontal partitioning with entropy and bi-fold measures, detects border irregularity using Sobel edge analysis, quantifies color with six RGB triplets and Euclidean thresholds, and converts diameter from pixels to millimeters. Dermoscopic images were also used in [12] to extract asymmetry through diagonal partitioning, evaluate border irregularity across eight regions, combine color occurrence with RGB statistics, and interpret diameter relative to the 6 mm threshold. Likewise, [7] applies the ABCD rule using shape/color asymmetry, eight-region border analysis, and RGB-based quantification of six color hues. More recent dermoscopy-based studies preserve the same interpretability while integrating learning-based classification stages. For example, paper [8] combines lesion segmentation, explicit ABCD feature extraction, and artificial neural networks for skin tumor classification using dermoscopic images. Lesion evolution can be quantified by using sequential dermoscopic analysis by capturing the changes in morphology and color over time [15]. Recent deep learning methodologies attempted to maintain interpretability by also predicting lesion classification and clinically significant ABCDE criteria from dermoscopic images [6].

On the other hand, approaches based on non-dermoscopic images are significantly limited and encounter more limitations. The study [1] proposed a two-stage methodology for standard camera images, adjusting the ABCD rule. Rather than using the classical dermoscopic formulation, their framework implemented a large set of geometric, gradient-based, and statistical color descriptors.

The ABCD rule is commonly used in dermoscopic imaging, but its direct application to standard RGB images remains problematic due to inconsistencies

in acquisition conditions, which can alter color consistency and feature reliability. In this context, we propose a clinically inspired approximation of ABCD features for standard RGB images captured in real-world clinical settings, thus improving dermatological interpretability beyond dermoscopy. The main question is whether ABCD-derived features can maintain diagnostically significant patterns in the absence of dermoscopic structures. Instead of directly copying dermoscopic criteria, we change them so that they still mean the same thing when it comes to asymmetry, border irregularity, color variation, and diameter, while also taking into account the differences that come with standard RGB imaging.

An important aspect of this work was the development of a feature extraction pipeline that can handle changes in lighting and color, which are difficult to avoid in diverse clinical settings. Non-dermoscopic imaging has a lot of differences in lighting, color balance, and reflectance, which differ significantly from dermoscopic systems, where acquisition conditions are controlled. To address this, we propose a preprocessing and color modeling method that is illumination agnostic by using gray-world normalization, reference-based white balance, and color calibration.

The proposed method ensures that the ABCD criteria can be adapted to standard RGB imaging by modeling each feature accordingly. A reference marker ensures the computation of the diameter in millimeters, while the measures based on contour and symmetry capture lesion morphology. The color variation is computed using a hybrid approach that can determine color patterns in non-dermoscopic images by using dermoscopic knowledge.

Overall, the proposed method allows the development of low-cost, easy-to-understand tools for melanoma screening by showing that ABCD-derived features can still show meaningful diagnostic trends without dermoscopic detail. This is especially important for use in a variety of clinical settings where standardized imaging is not always available and the ability to handle acquisition variability is crucial.

2 Methodology

This study proposes a framework for the assessment of melanocytic lesions based on the ABCD rule of dermatology using standard RGB images. Unlike conventional approaches relying on dermoscopic imaging, the proposed method operates on images acquired with a standard camera at an approximate distance of 40 cm. The framework extracts and quantifies the four components of the ABCD rule, computes the TDS, and enables the identification of the blue veil for lesion classification (see Fig. 1).

2.1 Data Acquisition

The images used in this study were acquired using the MelanoDet system, first presented in [13]. MelanoDet (Fig. 2) is a multispectral imaging platform com-

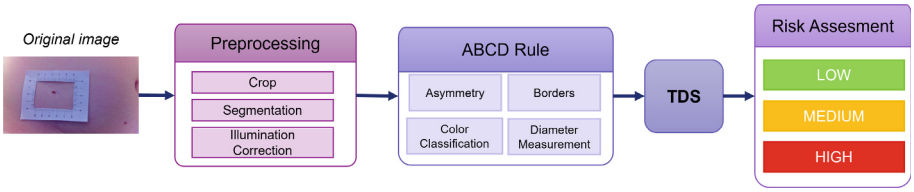

Fig. 1. Schematic diagram of the proposed method.

prising three cameras operating in different spectral ranges: visible (VIS), near-infrared (NIR), and long-wavelength infrared (LWIR, thermal imaging).

In this work, only the VIS modality was considered. A key advantage of the VIS camera within this system is its ability to support accurate lesion localization and to provide detailed morphological information, including color distribution, shape, and lesion area. These features enable the extraction of clinically relevant descriptors that contribute to the differentiation between benign and dysplastic lesions.

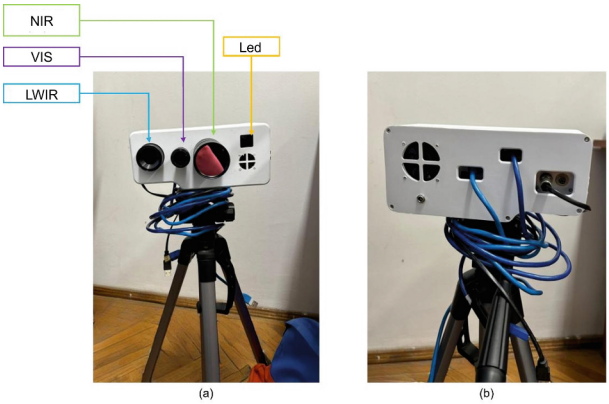

Fig. 2. MelanoDet imaging system.

Since this study focuses on non-dermoscopic RGB images, only the VIS camera specifications are considered. The camera module has a resolution of 1920×1080 pixels and is based on a 1/2" Sony IMX385 CMOS sensor, offering high sensitivity and high dynamic range (HDR). It provides a wide field of view (DFOV: 122°, HFOV: 110°) and supports object detection at working distances from approximately 30 cm to infinity. The module is equipped with an RGB M12-mount varifocal lens that allows manual focus adjustment.

2.2 Dataset

The dataset used in this study was acquired using a multispectral device presented in [13], over a period of 11 months, in collaboration with the Central

Military Emergency University Hospital "Dr. Carol Davila", Bucharest, Romania, and St. John's University Hospital, Bucharest, Romania. All participants provided informed consent, and the study was conducted in accordance with the Declaration of Helsinki (1975, revised 2004) and approved by the National University of Science and Technology POLITEHNICA Bucharest, University Ethics Committee, Subcommittee for Research Ethics (approval no. 26/06.10.2025).

The images were acquired from 40 cm, which ensured a consistent field of view across patients, without the need of magnification. In addition, for each patient a reference marker was used to enclose the lesion with the final purpose of localizing the lesion and perform the conversion from pixels to mm. Since the image acquisition was performed in a clinical setting, the illumination conditions were not controlled. This resulted in variability across images in terms of lighting, but consistent in positioning and framing of the lesion.

A total of 146 cases were collected, with diagnoses established either by experienced dermatologists or through histopathological analysis. For each case, three images were acquired in the VIS, NIR, and LWIR spectra, resulting in a total of 438 images. The dataset is categorized into three lesion classes: nevus (NV), dysplastic nevus (DN), and melanoma (MM). The sample distribution for each class is depicted in Fig. 3. In line with the objective of this study, which focuses on applying the ABCD rule to non-dermoscopic imaging, only VIS images were selected for further analysis.

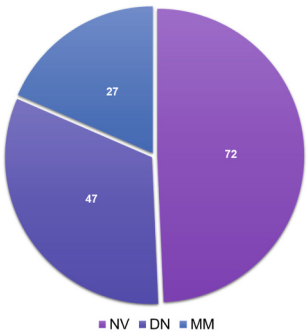

Fig. 3. Class distribution within the dataset.

2.3 Preprocessing

Since the images were acquired using an RGB camera in a clinical environment, where strict illumination control is difficult to enforce, a preprocessing pipeline was introduced to reduce variability in lighting and ensure color consistency across the dataset.

Lesion localization was performed via an initial cropping step using a pretrained YOLOv8n object detection model. Initialized with COCO weights and

fine-tuned on 50 manually annotated images to detect the reference marker, the model was trained on the VIS modality with data augmentation for 20 epochs. During inference, predictions were filtered with a 0.5 confidence threshold and 0.3 IoU-based non-maximum suppression; the highest-confidence bounding box was selected, expanded by a factor of 1.2, and used to extract the Region of Interest (ROI) for subsequent processing.

An illumination correction step was applied, combining gray-world color constancy with white balance adjustment. The gray-world assumption normalized the global color distribution to reduce color cast, after which white balance was performed relative to the red channel to preserve the natural color of human skin. The reference marker in each image was used to identify a white reference region (bright areas were detected via intensity thresholding, and candidate patches were extracted from the marker). From the patches extracted, the most neutral one (where there was minimal variation in the R,G,B channels mean) was selected as a reference for the white balance processing. Since the skin is characterized by red tones, we further computed the scaling factors for the green and blue channels relative to the red channel, and applied them to the entire image.

Since most of the images in the dataset contain small or low-contrasted lesions, automated segmentation methods were not reliable. Hence, we manually segmented each image and created masks using Adobe Photoshop. To ensure that the final mask contained only the lesion, we further applied a morphological erosion with a 5×5 structuring element.

2.4 ABCD Rule

The ABCD rule of dermatology is a widely used clinical guideline for the assessment of melanocytic skin lesions and early detection of melanoma. It is based on four criteria, each reflecting structural characteristics associated with malignancy.

Asymmetry (A) Asymmetry was determined along the vertical and horizontal axes, using a crop of the lesion mask which was further divided in two halves, corresponding to each axes.

Vertical asymmetry was computed by splitting the lesion into the left half (L) and the right half (R). The right half was flipped and compared to the left half by measuring how much they overlapped:

$$A_v = 1 - \frac{|L \cap R|}{|L \cup R|} \tag{1}$$

A similar process was performed for the horizontal asymmetry, where the lesion was divided into a top half (T) and a bottom half (B):

$$A_h = 1 - \frac{|T \cap B|}{|T \cup B|} \tag{2}$$

The overall asymmetry measure (A_{mean}) was defined as:

$$A_{mean} = \frac{A_v + A_h}{2} \tag{3}$$

We used a search process to find two thresholds (t_1, t_2) that would allow the mapping of the overall asymmetry values to the ABCD scoring system. In particular, all possible thresholds were evenly sampled in the $[0, 1]$ range, and all valid pairs (t_1, t_2), $t_2 > t_1$ were verified. We calculated the asymmetry score for all lesions in each pair and then compared the ABCD-based classification to the ground-truth labels. The best thresholds were chosen as those that gave the dataset the highest overall classification accuracy. Thus, the final values were $t_1 = 0.4$ and $t_2 = 0.7$.

Using the determined thresholds and considering that the asymmetry score ranges between 0 and 2, the final score A was defined as 0 if $A_{mean} < t_1$, 1 if $t_1 \leq A_{mean} < t_2$, and 2 if $A_{mean} \geq t_2$ [16].

Border Irregularity (B). Border irregularity was quantified using two complementary shape descriptors computed from the binary lesion mask: convexity irregularity and radial distance variation.

First, the external contour of the lesion was extracted, and the largest contour was retained for analysis. To measure global deviation from a regular shape, the convex hull of the lesion contour was computed. The convexity irregularity was then defined as

$$I_c = \frac{A_{\text{hull}} - A_{\text{lesion}}}{A_{\text{hull}}}, \tag{4}$$

where A_{lesion} is the contour area of the lesion and A_{hull} is the area of its convex hull.

To assess variations in the local contour, the centroid of the lesion was calculated using contour moments, and the Euclidean distance from the centroid to each contour point was evaluated. The coefficient of variation of the radial distances was employed to characterize the radial irregularity:

$$I_r = \frac{\sigma(d)}{\mu(d)}, \tag{5}$$

where $\sigma(d)$ and $\mu(d)$ represent the standard deviation and mean of the set of radial distances.

The final border irregularity measure was obtained by equally combining I_c and I_r:

$$I_b = 0.5 \cdot I_c + 0.5 \cdot I_r. \tag{6}$$

Finally, linear rescaling was used to map the continuous irregularity score to the ABCD border scale. The resulting value was then clipped to the interval $[0, 7]$, which lets it match the standard ABCD scoring range for border irregularity and be directly integrated into TDS [16].

Color (C). The first color analysis used six clinically important dermoscopic colors: white, red, light brown, dark brown, blue-gray, and black. These colors are often used in dermatological evaluations and are described in the literature with reference RGB triplets and their corresponding thresholds.

To perform color classification, we used a reference RGB triplet along with a RGB threshold for each of the six colors analyzed. If the Euclidean distance between a pixel's normalized RGB value and the reference color was less than the threshold, the pixel was assigned to that color [16].

Table 1 shows a summary of the reference values and thresholds that were used in the first implementation.

Table 1. RGB triplets used as reference and thresholds for the six known dermoscopic colors [16]

Color	Reference	Threshold
White	(1, 1, 1)	(0.8039, 0.8039, 0.8039)
Red	(0.8, 0.2, 0.2)	(0.5882, 0.1961, 0.1961)
Light Brown	(0.6, 0.4, 0.25)	(0.5882, 0.1961, 0)
Dark Brown	(0.4, 0.26, 0.13)	(0.1961, 0, 0)
Blue Gray	(0.2, 0.6, 1)	(0, 0.3922, 0.5882)
Black	(0, 0, 0)	(0.1961, 0.1961, 0.1961)

Practically, for each pixel p and color reference c_k, the distance was computed as:

$$d_k = \|p - c_k\|_2 \tag{7}$$

A pixel was assigned to color k if:

$$d_k \leq T_k \tag{8}$$

where T_k represents the threshold associated with the color k [16].

These reference values are established for dermoscopic images obtained under controlled conditions; however, this study utilized standard RGB images captured at 40 cm under clinical conditions, resulting in variability in illumination, color balance, and sensor response. As a result, direct application caused problems, such as misclassifying red and brown tones and not being able to find blue-gray areas very well. This led to a data-driven color refinement strategy.

Hybrid Color Classification To adapt dermoscopic color definitions to non-dermoscopic images, a data-driven calibration was performed using color quantization, where K-means clustering was applied to lesion pixels to extract dominant colors and refine RGB triplets. Color assignment thresholds were then empirically determined from pixel-reference distance distributions, balancing sensitivity and specificity while minimizing noise.

A hybrid classification strategy was employed, in which an initial rule-based stage defined color categories using RGB channel relationships, with red characterized by a dominant R channel and sufficient saturation while excluding brown-like patterns, brown tones by $R > G > B$, blue-gray by $B > R$ and $B > G$, and black or white determined using intensity-based thresholds. Pixels not classified in this stage were assigned using Euclidean distance to reference colors.

To reduce the effect of noisy pixels on color identification, a relative threshold based on the lesion area was added. Colors that made up less than a certain percentage of the lesion were left out because they were very few and still counted as separate colors. We looked at a few different thresholds (0%, 0.3%, 0.5%, and 0.8%) to see how they affected the final TDS and the performance of the classification.

Finally, the color score C was defined as the number of distinct colors present after applying the proposed classification algorithm, with the C score ranging from 1–6 [16].

Color Uniformity. We also determined the color uniformity to see how the colors were spread out in the lesion based on the number of pixels assigned to each color. If a dominant color covered more than 75% of the lesion area or more than 60% of the area with the second most common color below 30%, the lesion was considered uniform. This measure shows how similar the colors are. Most of the time, benign lesions have colors that are more even, while melanoma has colors that are more varied. Even though it wasn't part of the traditional ABCD rule, this metric was used to help figure out how colors changed.

Diameter. The lesion diameter was estimated using the equivalent diameter derived from the lesion area:

$$D_{px} = \sqrt{\frac{4A}{\pi}} \tag{9}$$

The diameter was converted from pixels to millimeters using a calibration factor:

$$D_{mm} = \frac{D_{px}}{\text{pixels per mm}} \tag{10}$$

The conversion from pixels to millimeters was based on the reference marker in each image and set to 9 pixels/mm. The ABCD rule was then used to break the lesion diameter down into ordinal categories. Scores $D \in [1, 6]$ were given based on D_{mm}, with $D = 1$ for $D_{mm} \leq 1$ and $D = 6$ for $D_{mm} > 5$, and so on for the middle intervals [16].

2.5 Rule Scoring

The TDS was computed as a weighted sum of the determined ABCD scores:

$$TDS = 1.3 \cdot A + 0.1 \cdot B + 0.5 \cdot C + 0.5 \cdot D \tag{11}$$

These weights were adopted from the standard ABCD rule formulation in dermatology, and the final classification was defined as NV if $TDS < 4.75$, DN if $4.75 \leq TDS \leq 5.75$, and MM if $TDS > 5.75$ [9].

3 Results

To be able to localize the lesion and anonymize the data, a cropping step was performed using the YOLOv8n object detection model. YOLOv8n was trained for 20 epochs with an 80/20 split for training and validation steps. The performance was evaluated using mAP_{5095}, mAP_{50}, mAP_{75}, mean F1-score, and per-class average precision (AP). The obtained results are summarized in Table 2.

Table 2. Validation metrics of the YOLOv8n model

$\text{mAP}_5 0-95$	mAP_{50}	mAP_{75}	F1	AP
0.8220	0.9800	0.9063	0.9472	0.8220

The high mAP_{50} value of 0.98 reported in Table 2 indicates good localization capability, while the mAP_{5095} score of 0.8220 reflects robust performance across varying IoU thresholds. The F1-score of 0.9472 further confirms a favorable balance between precision and recall, demonstrating reliable detection of the reference marker.

The effect of the preprocessing pipeline was evaluated by analyzing the impact of illumination correction. Gray-world normalization was applied to reduce the overall color cast in the images. Subsequently, reference-based white balancing further improved color consistency by adjusting the RGB channels according to a detected white region.

Qualitative analysis shows that the suggested preprocessing pipeline (Fig. 4) makes the lesions look more consistent by eliminating color distortions that occur in different acquisition conditions. After correction, red and brown tones stand out more, and blue-gray areas are shown more clearly. This improvement makes it easier to classify colors accurately and then extract ABCD features.

3.1 Feature Analysis

The extracted ABCD features show consistent patterns across lesion categories. MM lesions exhibit the highest values across all components, while nevus NV lesions show the lowest, with DN falling in between.

Mean asymmetry increases from 0.388 for NV to 0.419 for DN and 0.567 for MM. Border irregularity follows a similar trend, with mean values of 1.167 (NV), 1.519 (DN), and 2.273 (MM). The number of detected colors also rises

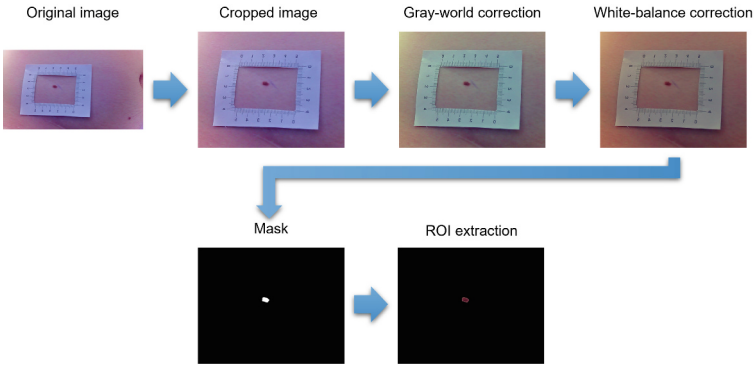

Fig. 4. Preprocessing pipeline.

progressively, from 2.778 (NV) to 3.538 (DN) and 4.045 (MM). Diameter shows the most pronounced separation, with melanoma reaching a mean of 7.995 mm, compared to 4.715 mm for DN and 2.723 mm for NV (Table 3).

Table 3. Mean values for the features extracted for each lesion class

Class	A	B	C	D
NV	0.388	1.167	2.778	2.723
DN	0.419	1.519	3.538	4.715
MM	0.567	2.273	4.045	7.995

To further validate the proposed framework, a qualitative analysis of the extracted ABCD features was performed. These examples highlight the ability of the method to capture clinically relevant characteristics across different lesion types.

Asymmetry. The asymmetry was analyzed by measuring how much the mirrored parts of the lesion overlapped along both the vertical and horizontal axes. NV lesions are usually symmetrical, with a lot of overlap between the two halves. On the other hand, MM lesions show clearer asymmetry, which is shown by less overlap and a more uneven distribution. DN possesses traits that are between benign and malignant patterns, as shown in Fig. 5.

Border Irregularity. Border irregularity was assessed by looking at both convexity deviation and radial distance variation. As demonstrated in Fig. 6, benign lesions usually have smooth, well-defined edges that are quite close to their convex hull. Melanoma lesions, on the other hand, have contours that are uneven, with big changes from convexity and more radial variance, which matches the real-life clinical scenarios.

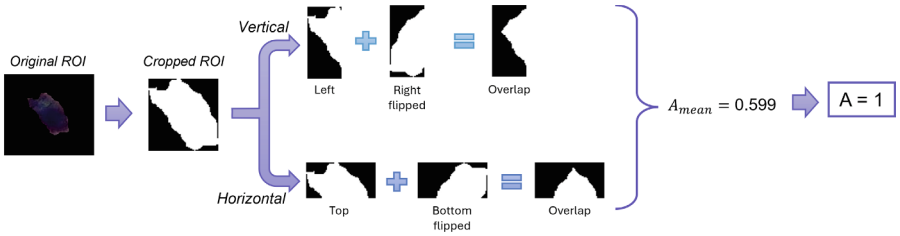

Fig. 5. Asymmetry score computed for a DN.

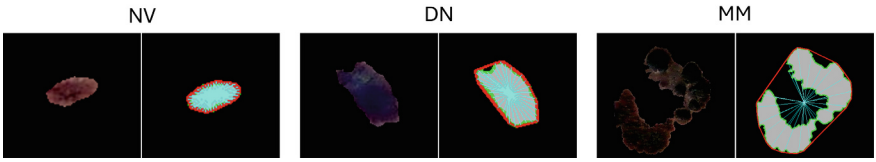

Fig. 6. Visualization of border irregularity for NV, DN, and MM.

Color Analysis. Color analysis confirms that melanoma lesions exhibit significantly higher chromatic heterogeneity compared to benign nevi, as seen in Table 4. The average number of detected colors increases from 2.778 (NV) to 4.045 (MM), reflecting the increased structural complexity of malignant lesions. Additionally, color uniformity decreases with lesion severity. NV exhibits higher uniformity, while MM shows the lowest values, indicating a more heterogeneous color distribution.

Table 4. Color statistics across lesion classes

Class	Mean Colors	Mean Uniformity
NV	2.778	0.681
DN	3.538	0.519
MM	4.045	0.364

Since the images were acquired under non-controlled conditions using a standard RGB camera and without polarized light, as in dermoscopic imaging, the reference RGB triplets and thresholds presented in Table 1 were not directly suitable for our dataset. Variations in illumination, reflections, and sensor response significantly affect color representation.

To address this limitation, a data-driven refinement of the color model was performed. Color quantization revealed that standard dermoscopic RGB triplets do not accurately represent the color distribution of non-dermoscopic images. In particular, blue-gray regions were often underrepresented, while red tones were frequently confused with brown shades (Fig. 7) due to illumination variability.

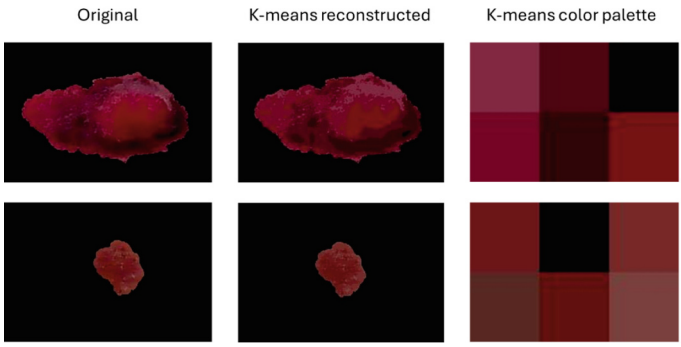

Fig. 7. Red color palette obtained through color quantization applied on the dataset. (Color figure online)

By applying K-means clustering to lesion pixels, dataset-specific color centroids were obtained, allowing refinement of reference triplets and thresholds. This step improved the consistency of color classification and enhanced the detection of clinically relevant features such as blue-gray structures. In Fig. 8, we show the 6 predominant colors in the entire dataset, lesions containing blue-gray or red components.



Fig. 8. Extracted color palette from the dataset, including blue-gray and red subsets. (Color figure online)

After determining the improved RGB triplets, we changed the reference and the threshold values for the following colors: red, light brown, and blue-gray. The improved RGB triplets can be seen in Fig. 9.

The hybrid color classification approach improved robustness by combining rule-based and distance-based methods, where the rule-based stage captured well-defined colors such as red and brown, and the distance-based stage ensured complete pixel assignment. An example is shown in Fig. 10, where blue-gray



Fig. 9. Comparison between dermoscopic reference color triplets and dataset-adapted RGB triplets.

regions were not detected using the original RGB triplets but were successfully identified after applying the proposed hybrid approach.

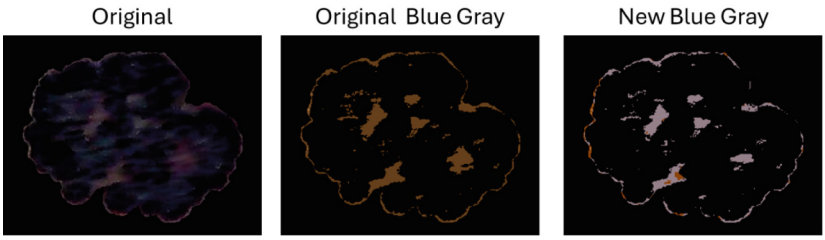

Fig. 10. Example of improved blue-gray detection after color quantization. (Color figure online)

The introduction of a relative noise threshold improved color stability by removing insignificant color components. Lower thresholds suppressed clinically relevant minor colors, whereas refined thresholds preserved diagnostically meaningful variations. As shown in Table 5, a threshold of 0.5 yielded the highest classification accuracy and was therefore adopted in the final hybrid color classification.

Table 5. Effect of noise threshold on classification performance

Threshold (%)	0	0.3	0.5	0.8
Accuracy (%)	68.49	69.18	70.55	68.49

3.2 Diameter

Diameter was estimated using the reference marker to convert pixel measurements into physical units. As illustrated in Fig. 11, melanoma lesions tend to

have larger diameters compared to NV, consistent with clinical guidelines. The use of a physical calibration marker ensures accurate and consistent measurement across all images.

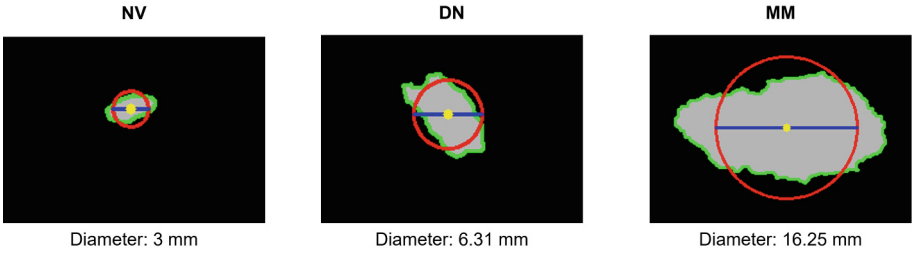

Fig. 11. Example of diameter computation.

3.3 Overall ABCD-Based Classification Performance

The proposed framework was evaluated on a dataset of 146 lesions, including 72 NV, 47 DN, and 27 MM cases. Using the computed ABCD features and the TDS, the method achieved an overall classification accuracy of 70.55%, with 103 correctly classified cases. A class-wise analysis shows that NV were classified with the highest accuracy, achieving 90.2%. MM cases reached a recall of 59.26%, while DN remained the most challenging class, with a recall of 46.81%. This behavior is consistent with clinical expectations, as DN represent an intermediate category with overlapping features between benign and malignant lesions, making them inherently more difficult to classify using rule-based approaches (Table 6).

Table 6. Classification performance per lesion type

	MM	DN	NV
Correct	16	22	65
Incorrect	11	25	7

To further evaluate the discriminative ability of the proposed framework, the continuous TDS values were analyzed using a ROC curve in a one-vs-rest setting, where melanoma cases were treated as the positive class and all remaining lesions as the negative class, as seen in Fig. 12. The ROC analysis showed an area under the curve (AUC) of 0.8358, which means that the TDS worked well at distinguishing the difference between images that were not dermoscopic. Youden's index showed that the best decision threshold was 5.7, which is similar to the threshold for MM detection that is accepted clinically. The method achieved 62.96% sensitivity and 94.12% specificity, revealing that the proposed method

can correctly determine non-melanoma lesions. These results show that the proposed ABCD-based framework performs well to keep the TDS's diagnostic value, even when used with standard RGB images.

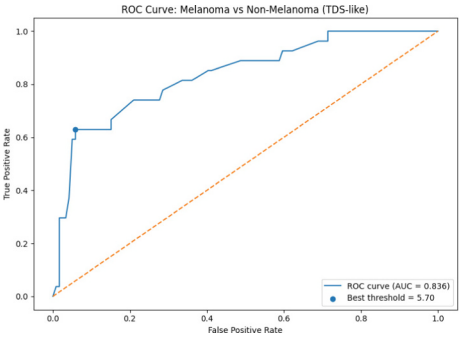

Fig. 12. ROC curve for MM versus non-MM classification using TDS.

Figure 13 shows how TDS values are dispersed across different types of lesions. The classes can be clearly separated because the mean TDS values are 3.42 for NV, 4.56 for DN, and 5.57 for MM. This gradual rise is expected from the ABCD rule in a clinical setting, where malignant lesions show more asymmetry, border irregularity, color variation, and diameter. The fact that DN overlaps with the other classes helps explain why this category had a lower classification performance.

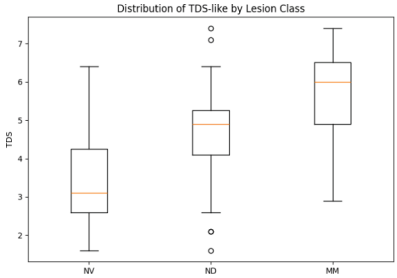

Fig. 13. TDS values distribution across lesion classes.

The suggested score does not seek to duplicate dermoscopic performance but to maintain clinically significant trends. In our dataset, all ABCD-derived components and the final score increase from NV to DN and MM. This shows that the adapted framework preserves the diagnostic structure in non-dermoscopic RGB images. The primary ambiguity occurs within the dysplastic category, aligning with its intermediate clinical characteristics.

These results suggest that ABCD-like features can provide useful support for dermatologists even in the absence of dermoscopic detail. However, the resulting

score is not directly equivalent to the dermoscopic TDS, as it is derived under different acquisition conditions and relies on more limited visible structures. Future work should focus on larger datasets, evaluating robustness under varying lighting conditions, and comparing the approach with both dermoscopic and learning-based methods.

4 Conclusions

This work presented a clinically-inspired approximation of ABCD feature extraction for non-dermoscopic RGB images acquired in realistic clinical conditions. Rather than directly reproducing dermoscopic TDS, the proposed framework investigates whether ABCD-derived descriptors can preserve diagnostically relevant trends when applied to standard visible-spectrum imaging. The results show that the adapted score captures meaningful differences between benign and malignant lesions, while also highlighting the difficulty of the dysplastic category. These findings support the potential of interpretable, low-cost RGB-based analysis as a complementary direction for melanoma screening in settings where dermoscopic imaging is not consistently available.

Acknowledgements. This work was supported by a grant of the Ministry of Research, Innovation and Digitization, CCDI-UEFISCDI, project number PN-IV-P7-7.1-PED-2024-1873, within PNCDI IV. The authors sincerely thank the hospitals and dermatologists for granting them access to acquire the necessary images for this study. They also extend their gratitude to all the volunteers who participated in this research and contributed to their work.

Disclosure of Interests. The authors have no competing interests to declare that are relevant to the content of this article.

References

1. Cavalcanti, P.G., Scharcanski, J., Baranoski, G.V.: A two-stage approach for discriminating melanocytic skin lesions using standard cameras. Expert Syst. Appl. **40**(10), 4054–4064 (2013)
2. Chatterjee, S., Dey, D., Munshi, S., Gorai, S.: Dermatological expert system implementing the ABCD rule of dermoscopy for skin disease identification. Expert Syst. Appl. **167**, 114204 (2021)
3. Hofman, M.S., Hicks, R.J.: Role of pet/ct in melanoma. In: PET/CT in melanoma, pp. 37–51. Springer (2017)
4. International Agency for Research on Cancer, World Health Organization: Global burden of cutaneous melanoma in 2020 and projections to 2040 (May 2022). https://www.iarc.who.int/infographics/global-burden-of-cutaneous-melanoma-in-2020-and-projections-to-2040/, Accessed 30 March 2026
5. Jartarkar, S.R., et al.: New diagnostic and imaging technologies in dermatology. J. Cosmet. Dermatol. **20**(12), 3782–3787 (2021)

6. Kotla, H., Rajasekaran, A.K., Rana, H.: A multi-task deep learning framework for skin lesion classification, ABCDE feature quantification, and evolution simulation, arXiv preprint arXiv:2510.14855 (2025)
7. Mabrouk, M.S., Sayed, A.Y., Afifi, H.M., Sheha, M.A., Sharwy, A.: Fully automated approach for early detection of pigmented skin lesion diagnosis using ABCD. J. Healthcare Inform. Res. **4**(2), 151–173 (2020)
8. Messadi, M., Cherifi, H., Bessaid, A.: Segmentation and ABCD rule extraction for skin tumors classification, arXiv preprint arXiv:2106.04372 (2021)
9. Pathan, S., Prabhu, K.G., Siddalingaswamy, P.: Techniques and algorithms for computer aided diagnosis of pigmented skin lesions–a review. Biomed. Signal Process. Control **39**, 237–262 (2018)
10. Pelagotti, A., Ferrara, P., Pescitelli, L., Gerlini, G., Piva, A., Borgognoni, L.: Non-invasive inspection of skin lesions via multispectral imaging. In: Optical Methods for Inspection, Characterization, and Imaging of Biomaterials, vol. 8792, pp. 55–67. SPIE (2013)
11. Roky, A.H., et al.: Overview of skin cancer types and prevalence rates across continents. Cancer Pathogenesis Therapy **3**(02), 89–100 (2025)
12. Senan, E.M., Jadhav, M.E.: Analysis of dermoscopy images by using ABCD rule for early detection of skin cancer. Global Transitions Proc. **2**(1), 1–7 (2021)
13. Sultana, A.E., Oniga, M., Rus, P.F., Dobre, A.L., Orzan, O.A.: Melanodet: multimodal imaging system for screening and analysis of cutaneous melanoma. IEEE Access (2025)
14. Thompson, J.F., Scolyer, R.A., Kefford, R.F.: Cutaneous melanoma. The Lancet **365**(9460), 687–701 (2005)
15. Yu, Z., et al.: Early melanoma diagnosis with sequential dermoscopic images. IEEE Trans. Med. Imaging **41**(3), 633–646 (2021)
16. Zaqout, I.: Diagnosis of skin lesions based on dermoscopic images using image processing techniques. Pattern Recognition-Selected Methods and Applications. IntechOpen (2019)